Supplementary Information

Global mapping of urban thermal anisotropy reveals substantial potential biases for remotely sensed urban climates

Huilin Du[a], Wenfeng Zhan[a, b*], Zihan Liu[a*], E. Scott Krayenhoff[c], TC Chakraborty[d], Lei Zhao[e], Lu Jiang[a], Pan Dong[a], Long Li[a], Fan Huang[a], Shasha Wang[a], Yuyue Xu[f]

a. *Jiangsu Provincial Key Laboratory of Geographic Information Science and Technology, International Institute for Earth System Science, Nanjing University, Nanjing 210023, China*
b. *Jiangsu Center for Collaborative Innovation in Geographical Information Resource Development and Application, Nanjing 210023, China*
c. *School of Environmental Sciences, University of Guelph, Guelph N1G 2W1, Canada*
d. *Atmospheric Sciences and Global Change Division, Pacific Northwest National Laboratory, Richland 99352, USA*
e. *Department of Civil and Environmental Engineering, University of Illinois at Urbana-Champaign, Urbana 61820, USA*
f. *School of Geography and Ocean Science, Nanjing University, Nanjing 210023, China*

*Corresponding author.

E-mail address: zhanwenfeng@nju.edu.cn (W. Zhan) and liuzihan_trs@foxmail.com (Z. Liu).

This file includes

A. Supplementary Notes

Supplementary Notes S1 to S4

B. Supplementary Figures

Supplementary Figures S1 to S17

C. Supplementary Table

Supplementary Table S1

D. Supplementary References

Supplementary References 1 to 19

A. Supplementary Notes

Note S1: *More details on the study area and data*

We chose a total of 5586 cities (each with an urban area in 2000 larger than 10 km^2) worldwide (Fig. S1). These cities are distributed in all the four typical climates according to the Köppen Climate Classification [1], including equatorial (458 cities), arid (897 cities), warm (2502 cities), and snow climates (1729 cities).

We employed Moderate Resolution Imaging Spectroradiometer (MODIS) data, reanalysis data, and auxiliary data to assist analysis. The Aqua and Terra MODIS data include daily land surface temperature (LST; the MYD11A1 and MOD11A1 products), yearly land cover type (MCD12Q1), and 16-day composite enhanced vegetation index

(EVI; MOD13A2). Most studies that use satellites to examine thermal anisotropy rely on instantaneous multi-angle LST observations obtained from geostationary meteorological satellites [2, 3]. However, the spatial resolution of the thermal images acquired from geostationary satellites is usually too coarse (~5 km) to isolate urban surfaces; and sensors from geostationary satellites cannot adequately detect the thermal status of polar regions. By contrast, thermal images acquired from polar orbiters (e.g., Aqua and Terra MODIS thermal data) are characterized by a relatively higher resolution (1 km) and they sample the Earth's surface more uniformly. For the same area, the MODIS viewing zenith angle (VZA) varies by day, but with a VZA repetition period of 16 days [4]. Therefore, the Aqua and Terra MODIS multi-angle LST observations (−65° ~ 65°) serve as unique sources for investigating urban thermal anisotropy (UTA) across global cities. The transit times for Aqua are around 13:30 and 01:30 local solar time, while those for Terra are around 10:30 and 22:30 local solar time. The MODIS land cover type data were employed to eliminate the water pixels as well as to examine the uncertainties related to the residual atmospheric effect from MODIS LST products. The land cover type data hold a spatial resolution of 500 m [5] and were resampled to 1 km to match the resolution of the LST products. The EVI data with a spatial resolution of 1 km were applied to analyze the relationships between UTA intensity (UTAI) and urban vegetation coverage.

The ERA5-land reanalysis data used here include the hourly surface air temperature (SAT) and downward shortwave radiation (RAD). These two types of data possess a grid of approximately 0.1 arc degree [6], and they were used to investigate the relationships between UTAI and air temperature and shortwave radiation across global cities. We converted the reanalysis SAT and RAD products, which are in Coordinated

Universal Time (UTC), to local solar time to match the MODIS LST products [4].

The auxiliary data involve global urban boundary (GUB), global impervious surface percentage (ISP), and building height information across Europe, the United States, and China. To reduce the impacts of urbanization-induced land cover changes on the UTAI characterization, we only kept the urban surfaces within the GUB data of 2000 [7]. The ISP data were obtained from Global Human Settlement Layers (GHSL) Built-Up Grid dataset and were also aggregated to 1 km from their original 38 m resolution [8]. The building height data at 1 km resolution were provided by ref. [9]. Both the ISP and building height data were used to analyze the relationship between UTAI and urban surface properties across global cities.

Note S2: ***More details on the calculation of UTAI across global cities and uncertainties related to UTAI calculation***

We developed a systematic approach to quantify the UTAI across global cities. First, we selected clear-sky pixels by removing pixels with a missing data rate exceeding 90% due to cloud contamination [10]. Second, we binned the MODIS VZAs (−65° ~ 65°) into 13 groups with an interval of 10° for each group. The LST observations for each VZA bin were all averaged to reduce uncertainties arising from retrieval errors of satellite-derived LSTs [11]. We kept only the VZA groups with less than 85% missing pixels, because an extremely high missing rate may drastically bias the UTAI quantification. Third, we employed a quadratic curve with the quadratic coefficient less than 0 to fit the LST variations with sensor VZAs once the number of valid VZA groups exceeded 10 after data screening to reduce the LST fluctuations and to obtain a more representative UTA curve at the city scale. Finally, we represented the UTAI as the

maximum difference between the nadir and off-nadir LSTs [12].

One may question that the selection of thresholds in abovementioned procedures could lead to uncertainties on the UTAI calculation. In addition, we have incorporated all valid MODIS multi-angle LST records during the period from 2003 to 2021. One may additionally argue that urbanization during this period may change urban surface properties and consequently affect the UTAI calculation. To examine the potential uncertainties, we further analyzed the UTAI variations with different thresholds, including filtering clear-sky pixels (termed threshold-1; ranging from 0.95 to 0.60), selecting usable sensor VZA intervals (termed threshold-2; ranging from 0.95 to 0.60), and choosing eligible cities (termed threshold-3; ranging from 6 to 13). We also examined the urbanization-induced impacts on UTAI calculation using different lengths of the study period (from 5 to 18 years). The sensitivity analysis reveals that the UTAI rarely changes under different thresholds and study periods, with the UTAI varying by less than 3% referenced to the original baseline (Fig. S15).

Note S3: ***Uncertainties related to daily weather variability and residual atmospheric effects in MODIS LST products***

Daily weather variations caused by non-synchronous MODIS LST observations in different VZAs, together with the residual atmospheric effect from MODIS LST products, may introduce uncertainties to the UTAI quantification. We therefore further discussed these two potential uncertainties and we also performed cross-validations of the proposed method with previous methods [13, 14].

1. ***Possible uncertainties related to daily weather variability caused by***

non-synchronous satellite LST observations in different view zenith angles

This study employed MODIS multi-angle LST observations to investigate the UTA across global cities. Unlike the instantaneous LSTs obtained from airborne observations, geostationary satellites, or model simulations, the MODIS multi-angle instantaneous LSTs are usually non-synchronous and obtained on different days [11, 13]. Daily variations in weather conditions may therefore introduce uncertainties in the investigation of UTA intensity (UTAI). Nevertheless, we consider such uncertainties would barely invalidate our main findings, mainly due to the following three reasons. First, we have filtered clear-sky pixels and removed the sensor VZA groups with extremely high data missing rate to reduce the impacts of daily weather variabilities on UTAI quantification (refer to Supplementary Note S2). Second, we have averaged the valid LSTs of the same VZA for all available days within a specific season throughout an 18-year period, obtaining an adequate number (> 100 for this study) of LST observations for each VZA group. This temporal averaging process can substantially reduce the uncertainties induced by daily weather variabilities. Third, our study has been focused on the statistical UTAI features for thousands of cities worldwide or within a specific climate zone. The large-scale spatial averaging procedure could further suppress the possible uncertainties induced by daily weather variabilities according to the Bessel formula in error theory [15].

2. ***Uncertainties related to residual atmospheric effects in MODIS LST products***

The residual atmospheric effect in MODIS LST products indicates that the MODIS multi-angle LSTs may have been retrieved 'imperfectly' due to the less accurate correction or parameterization of the atmospheric path thermal radiance for different sensor VZAs [13, 16]. The residual atmospheric effect may impact the UTAI

investigation. We therefore further investigated the uncertainties induced by the residual atmospheric effect by examining the surface thermal anisotropy over 256 lakes larger than 30 km^2, as water bodies are usually considered to possess relatively low thermal anisotropy [13]. The results demonstrate that the thermal anisotropy intensity over water bodies is less than 2.0 K both during the day and at night (Fig. S16). This indeed suggests a slight impact from the residual atmospheric effects on UTAI quantification, yet such an intensity is substantially lower than the UTAI quantified in this study, especially during summer daytime (i.e., 5.1 K). This therefore supports that the residual atmospheric effect would not largely bias the main results of this study. Future endeavors may consider elimination of the residual atmospheric effect to better assess the UTAI across global cities.

3. *Cross-validation of the proposed method with previous methods*

Previous studies have made substantial progresses in suppressing or eliminating the uncertainties related to daily weather variabilities and residual atmospheric effects in UTAI quantification [13, 14]. For example, a pioneering attempt performed by ref. [13] eliminated these two uncertainties by means of high-quality measurements from weather stations within cities and large water bodies adjacent to cities. This approach is well accepted, but it is extremely difficult and even impossible to be extended to thousands of cities at a large scale, especially for cities over rugged terrain without large water bodies nearby. Recently, an innovative modification of this approach was made by removing the impacts from daily weather variabilities based on strong temporal correlations between LST and SAT, and by ignoring the impacts from residual atmospheric effects [14]. This modification overcame the necessity of adjacent water bodies required in ref. [13] and allowed the satellite-based examination of UTAI to be

applicable to inland cities worldwide.

To validate our method, we first compared the UTAI of Chicago and New York retrieved by our proposed method with that retrieved by ref. [13]. The results show that these two approaches unveil consistent UTAI patterns in Chicago and New York when ISP is less than 80% (Fig. S17). Nevertheless, our quantified UTAI (around 6.0 K) is slightly lower than that of ref. [13] (around 8.0 K) over highly urbanized surfaces (i.e., ISP > 80%) in New York. By employing a more stringent threshold for filtering clear-sky pixels, we found that the UTAI retrieved with our approach can increase to 7.6 K (Fig. S17b), which is very close to the UTAI given by ref. [13]. This strongly suggests that the discrepancy between these two approaches may be related to the different filtering criteria of clear-sky pixels, with the UTAI generally more pronounced under clearer sky conditions due to the stronger solar radiation (Fig. S6; ref. [11]). This also indirectly shows the validity of our proposed method for deriving UTAI. To involve as many cities as possible, this study retains a threshold of 0.9 for filtering clear-sky pixels.

We further compared the UTA curves and intensities between the current study and ref. [14] across 25 global cities during summer and winter daytime (Fig. S9). The results show that the UTAI quantified by this study are slightly larger than those by ref. [14] during both summer and winter. The patterns of UTA curves display a relatively good consistency between our study and ref. [14] during summer, while they become quite different during winter. The UTA curves of ref. [14] display a hotspot effect when the sensor VZA is large, while the hotspot occurs between +5° and +15° in the morning and between −25° and −15° in the afternoon in our study. These differences may be largely

attributed to the different methods used to remove the impacts from daily weather variabilities in each study. Our study eliminated such impacts through substantial temporal averaging processes based on the Bessel formula in error theory [15]; while ref. [14] removed such impacts by incorporating *in-situ* SAT measurements within cities. Additionally, the small magnitude of UTAI and the relatively low quality of LST observations during winter may also introduce potential uncertainties into UTAI quantification, leading to observational differences between the two studies during wintertime. Further investigations of global UTA patterns during winter through extensive cost-efficient and easily operable means (e.g., unmanned aerial vehicles) remain necessary [17].

Note S4: ***More details on the quantification of UTA-induced biases in typical urban climate variables across global cities***

The calculations of percentage biases in urban surface-emitted longwave radiation (E), latent heat flux (LE), sensible heat flux (H), and Bowen ratio (BR) are detailed as follows according to ref. [18]:

The percentage bias of E was calculated by the following formula:

$$\begin{cases} E_{\text{nadir}} = \varepsilon_{\text{s}} \cdot \sigma \cdot T_{\text{s\_nadir}}^{\ 4} \\ E_{\text{offnadir}} = \varepsilon_{\text{s}} \cdot \sigma \cdot T_{\text{s\_offnadir}}^{\ 4} \\ \text{bias}\% = \left(\frac{T_{\text{s\_offnadir}}^{\ 4}}{T_{\text{s\_nadir}}^{\ 4}} - 1\right) \times 100\% \end{cases} \quad (1)$$

where ε_{s} denotes the urban surface emissivity; σ represents the Stefan-Boltzmann constant (5.67×10^{-8} W·m^{-2}·K^{-4}); $T_{\text{s\_nadir}}$ and $T_{\text{s\_offnadir}}$ denote the LST (K) observed from nadir and off-nadir directions, respectively.

The percentage bias of *LE* was calculated by the following formula:

$$\begin{cases} LE_{\text{nadir}} = \lambda(T_{\text{a}}) \cdot g_{\text{c}} \cdot \beta \cdot \rho \cdot \dfrac{q_{\text{sat}}(T_{\text{s\_nadir}}) - q_{\text{a}}}{r_{\text{a}} + r_{\text{c}}} \\ LE_{\text{offnadir}} = \lambda(T_{\text{a}}) \cdot g_{\text{c}} \cdot \beta \cdot \rho \cdot \dfrac{q_{\text{sat}}(T_{\text{s\_offnadir}}) - q_{\text{a}}}{r_{\text{a}} + r_{\text{c}}} \\ \text{bias\%} = \left(\dfrac{q_{\text{sat}}(T_{\text{s\_offnadir}}) - q_{\text{a}}}{q_{\text{sat}}(T_{\text{s\_nadir}}) - q_{\text{a}}} - 1\right) \times 100\% \end{cases} \quad (2)$$

where $\lambda(T_{\text{a}})$ represents the latent heat of vaporization (J kg^{-1}) and is a function of near-surface air temperature (T_{a}). T_{a} was calculated based on the ERA5 reanalysis data; g_{c} represents the vegetation coverage of urban surfaces; β represents the water stress factor; ρ is the mean air density (kg m^{-3}); r_{a} and r_{c} represent the aerodynamic resistance (s m^{-1}) and vegetation canopy resistance (s m^{-1}), respectively; $q_{\text{sat}}(T_{\text{s}})$ denotes the specific humidity at saturation (kg kg^{-1}) and was calculated as $0.622 \times \dfrac{\text{e}_{\text{sat}}(T_{\text{s}})}{p_{\text{atm}} - 0.378 \times \text{e}_{\text{sat}}(T_{\text{s}})}$, where p_{atm} denotes the atmospheric pressure from reanalysis data, and $\text{e}_{\text{sat}}(T_{\text{s}}) = 0.6108 \times \text{e}^{\frac{17.27 \times T_{\text{s}}}{T_{\text{s}} + 237.3}}$ (k Pa); and q_{a} denotes the specific humidity of air (kg kg^{-1}) calculated based on reanalysis product.

By simplifying the 3D geometry of urban surfaces, the percentage bias of *H* was calculated as:

$$\begin{cases} H_{\text{nadir}} = \rho \cdot c_{\text{p}}(T_{\text{a}}) \cdot \dfrac{T_{\text{s\_nadir}} - T_{\text{a}}}{r_{\text{a}} + r_{\text{ah}}} \\ H_{\text{offnadir}} = \rho \cdot c_{\text{p}}(T_{\text{a}}) \cdot \dfrac{T_{\text{s\_offnadir}} - T_{\text{a}}}{r_{\text{a}} + r_{\text{ah}}} \\ \text{bias\%} = \left(\dfrac{T_{\text{s\_offnadir}} - T_{\text{a}}}{T_{\text{s\_nadir}} - T_{\text{a}}} - 1\right) \times 100\% \end{cases} \quad (3)$$

where $c_p(T_a)$ represents the specific heat of dry air at constant pressure (J kg^{-1} K^{-1}) and is a function of T_a; and r_{ah} denotes the radiometric excess resistance [19].

The percentage bias of *BR* (i.e., the ratio of *H* to *LE*) was therefore given by:

$$\text{bias}\% = \left(\frac{\frac{T_{\text{s\_offnadir}} - T_a}{q_{\text{sat}}(T_{\text{s\_offnadir}}) - q_a}}{\frac{T_{\text{s\_nadir}} - T_a}{q_{\text{sat}}(T_{\text{s\_nadir}}) - q_a}} - 1\right) \times 100\% \tag{4}$$

I_s was calculated by the following formula:

$$\begin{cases} I_{\text{s\_nadir}} = T_{\text{s\_urban}}(0°) - T_{\text{s\_rural}}(0°) \\ I_{\text{s\_offnadir}}(\theta) = T_{\text{s\_urban}}(\theta) - T_{\text{s\_rural}}(\theta) \\ \text{bias}\% = \left(\frac{T_{\text{s\_urban}}(\theta) - T_{\text{s\_rural}}(\theta)}{T_{\text{s\_urban}}(0°) - T_{\text{s\_rural}}(0°)} - 1\right) \times 100\% \end{cases} \tag{5}$$

where $I_s(\theta)$ signifies the surface UHI intensity at the sensor VZA of θ; and $T_{\text{s\_urban}}(\theta)$ represents the urban mean LST while $T_{\text{s\_rural}}(\theta)$ represents the rural mean LST when the sensor VZA is θ.

B. Supplementary Figures

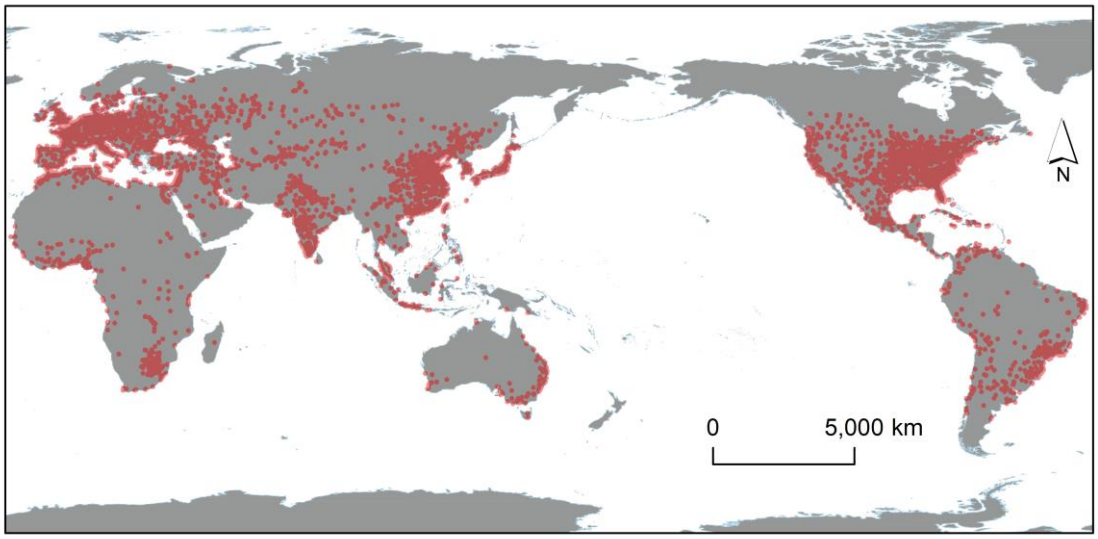

审图号: GS京(2023)1053号

Fig. S1. Distribution of the chosen 5586 cities worldwide.

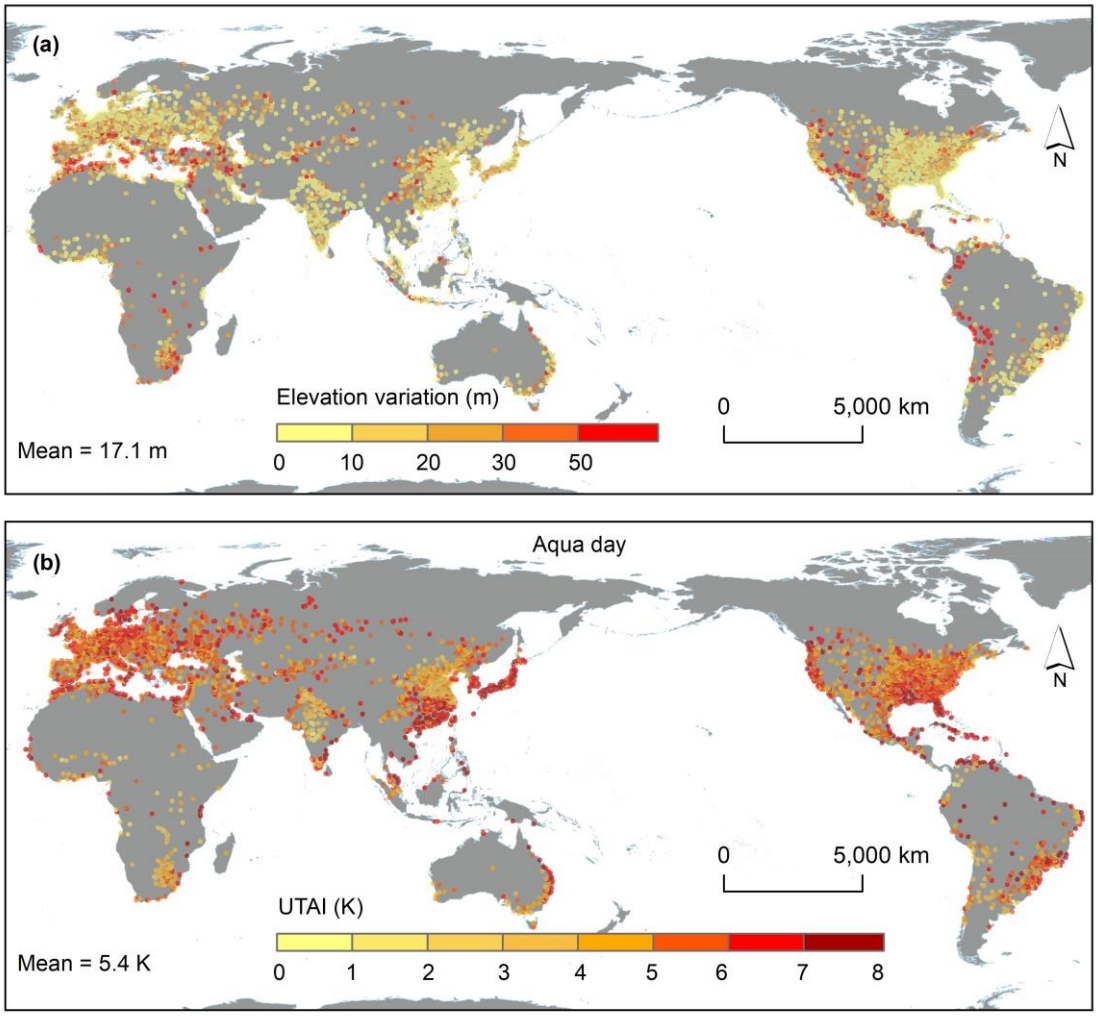

审图号: GS京(2023)1053号

Fig. S2. The intra-city elevation variation across global cities (a) and the global UTAI pattern calculated based only on pixels with elevation within ± 50 m of the median elevation of urban pixels during summer daytime (b).

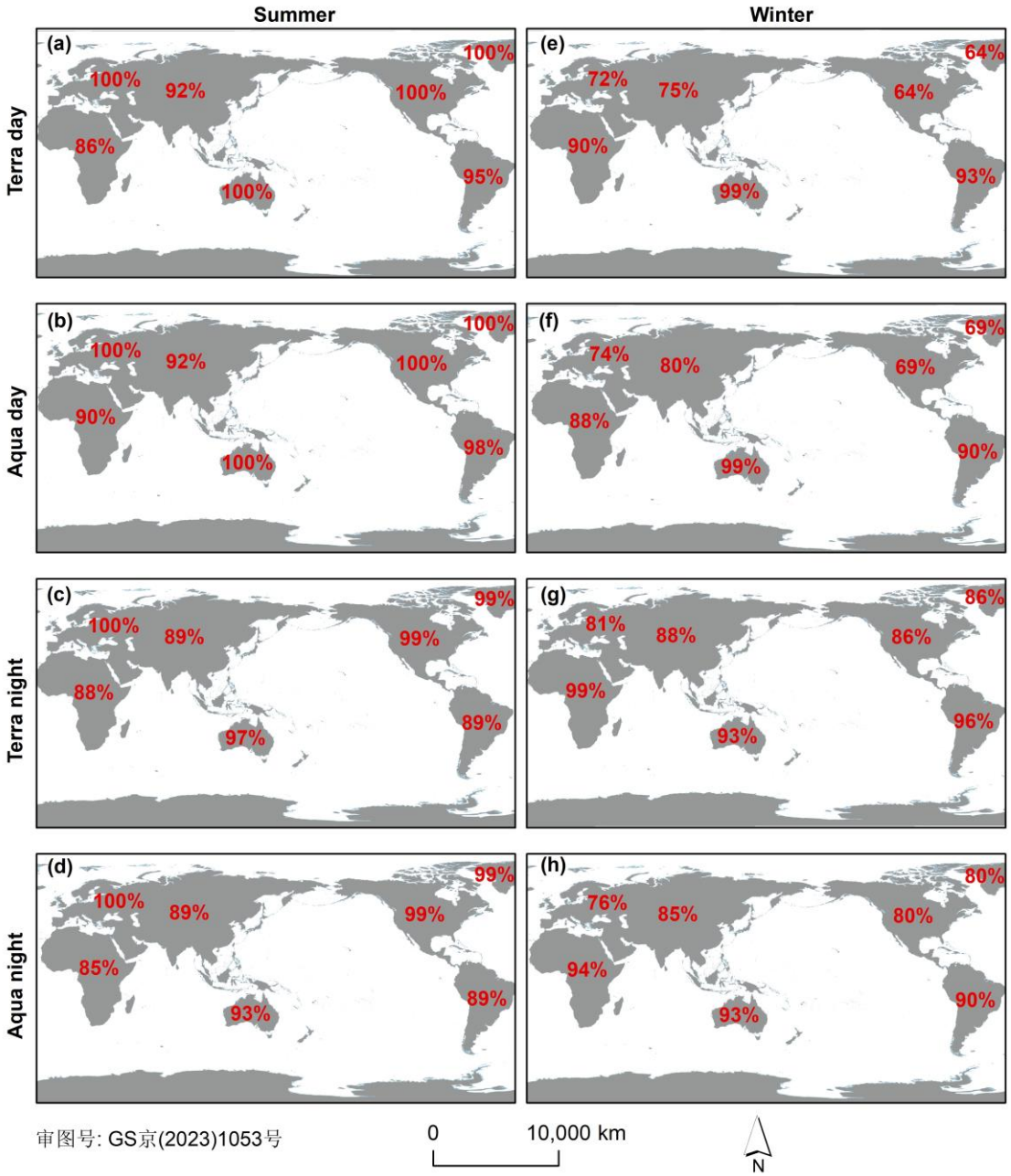

Fig. S3. Relative representations of cities used for UTAI investigation across various continents at different observation time nodes | The city representability was calculated as the ratio of the number of the final selected cities used for the UTAI investigation to the number of the original chosen cities.

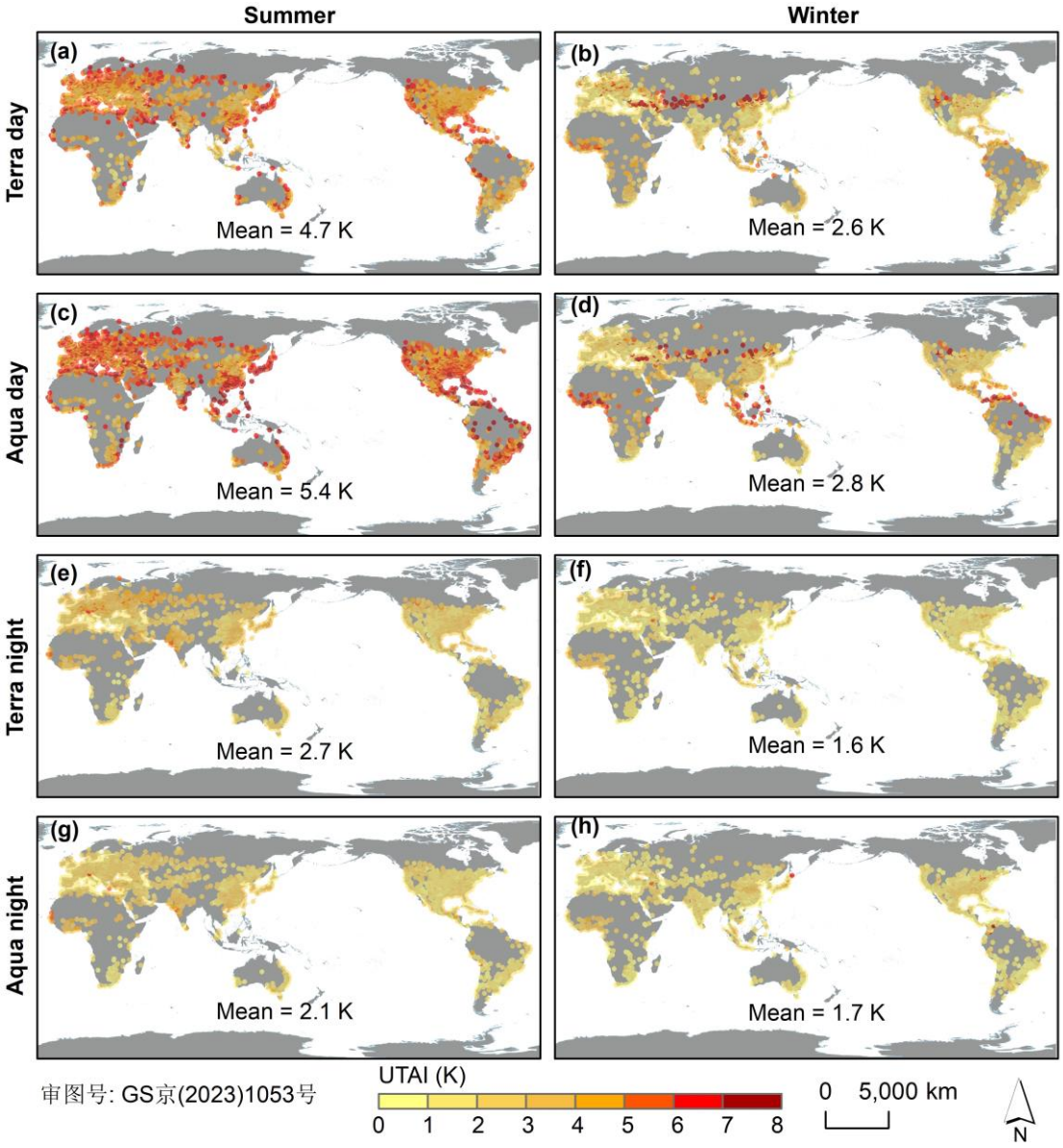

Fig. S4. Spatiotemporal patterns of UTAI across global cities | The global UTAI pattern during the day (**a** to **d**) and at night (**e** to **h**), with the values in each subgraph denoting the global mean UTAI at different time nodes. The first and second columns denote summer and winter, respectively.

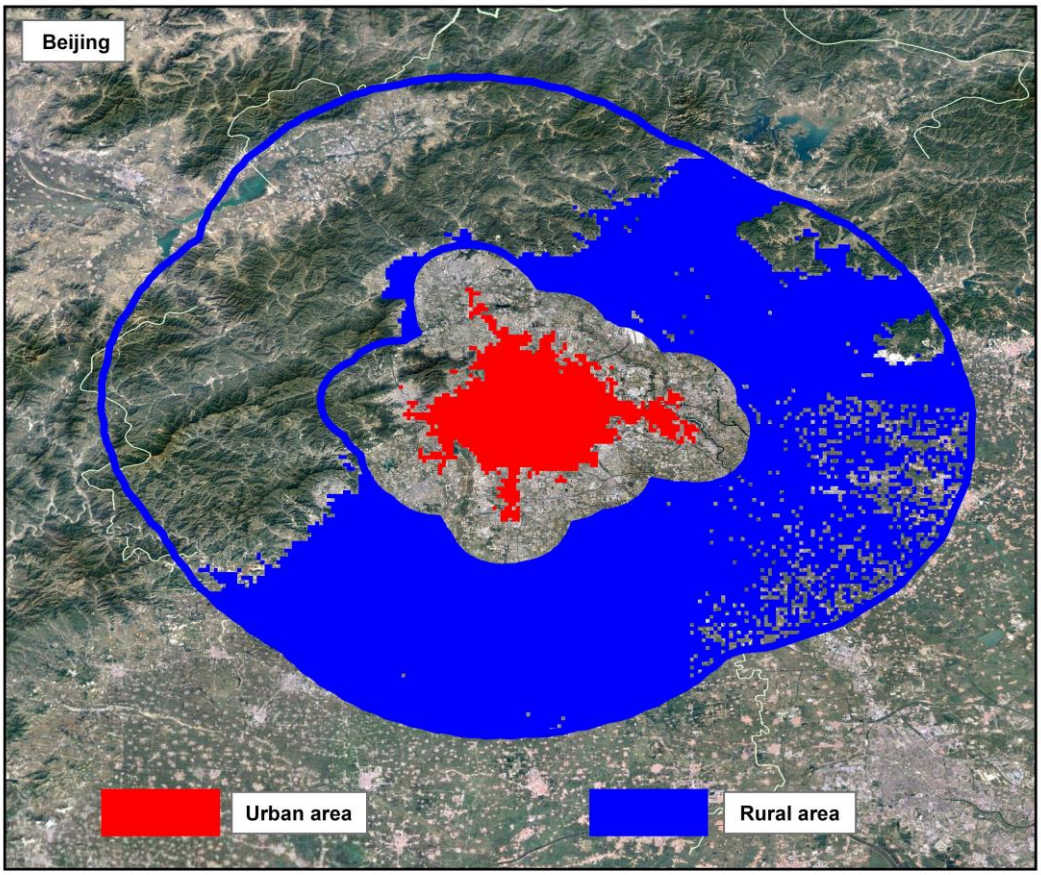

Fig. S5. Illustration of the urban area (red color) and rural area (blue color) | The rural area is delineated as the ring area between 10-km and 50-km buffer zone outside the corresponding urban area). The pixels beyond ± 50 m of the median elevation of each city and those identified as 'urban and built-up' were further discarded to more reasonably delineate rural surfaces.

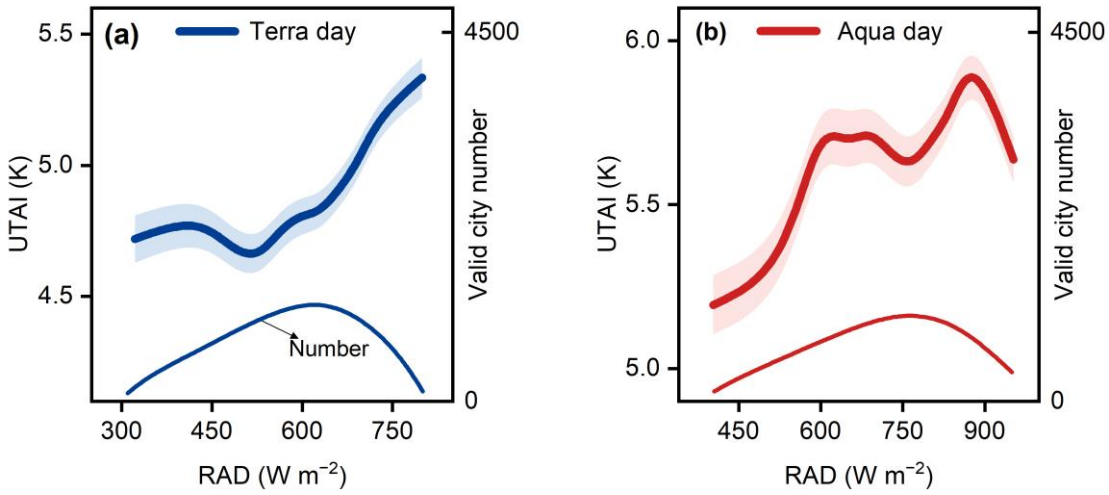

Fig. S6. The variations of UTAI along with the downward solar radiation (RAD; unit: W/m^2) across global cities | The shadings represent the standard errors of the UTAI. The relatively large variation of RAD arises from both latitudinal and intra-seasonal variations of RAD.

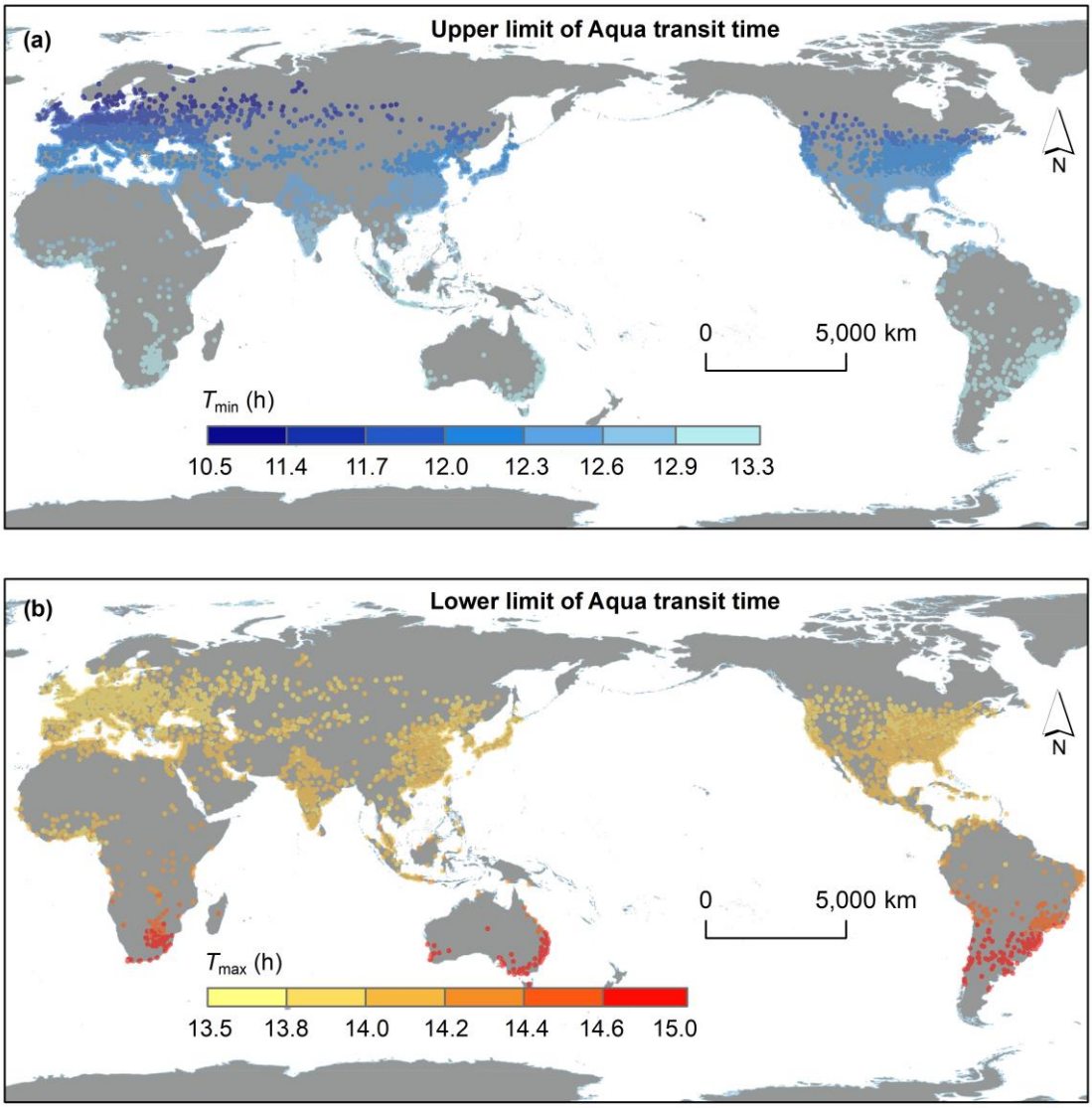

Fig. S7. Upper (a) and lower (b) limits of the transit time range (termed T_{max} and T_{min}, respectively) for Aqua satellite during summer daytime across global cities | The transit time is retrieved from the 'Day_view_time' band of MYD11A1 product.

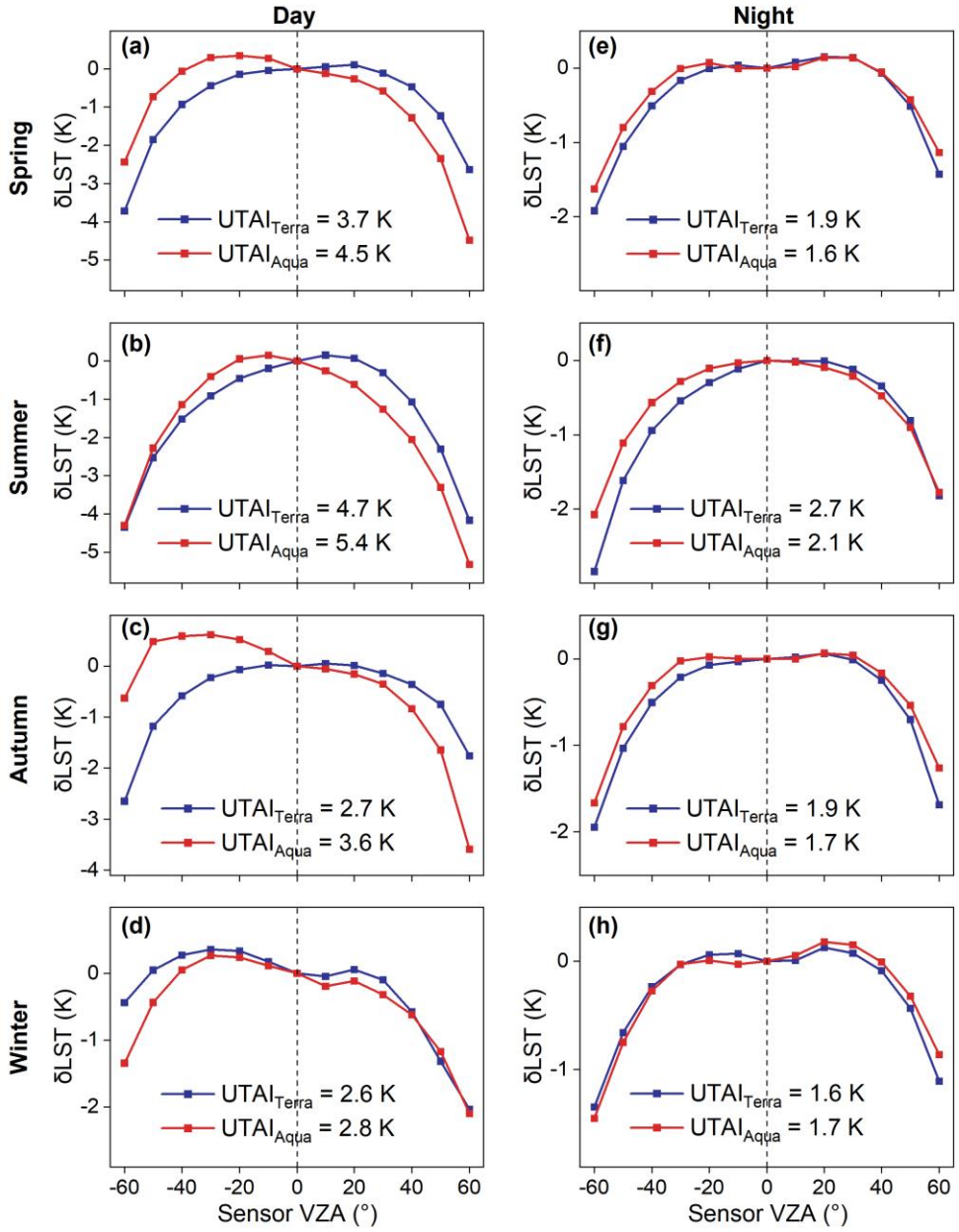

Fig. S8. Global mean urban thermal anisotropy (UTA) curves for the four seasons | The $UTAI_{Terra}$ and $UTAI_{Aqua}$ denote the Terra- and Aqua- based UTA intensity (UTAI), respectively, and the δLST represents the difference between off-nadir and nadir LST. For cities in the northern hemisphere, spring, summer, autumn, and winter were defined as March to May, June to August, September to November, and December to February, respectively; and vice versa for cities in the southern hemisphere.

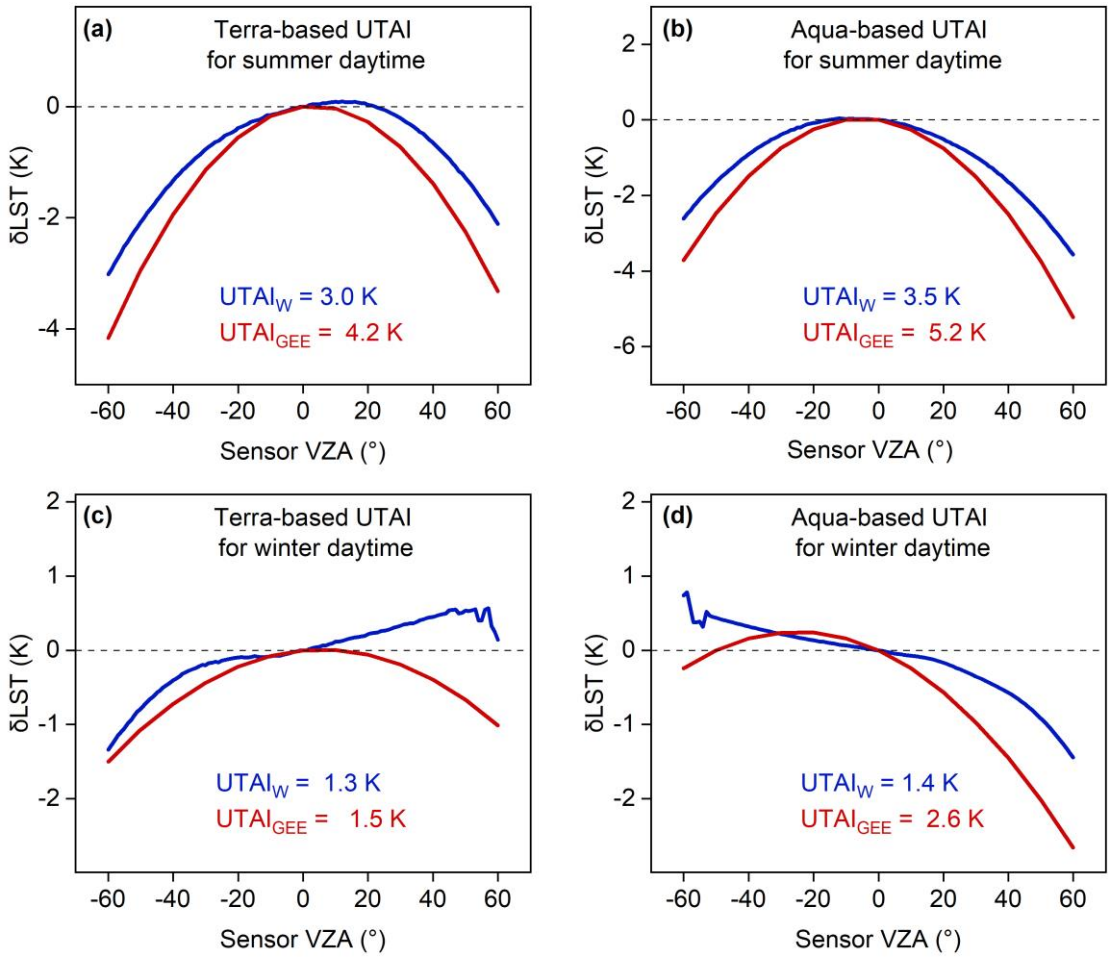

Fig. S9. Comparisons of urban thermal anisotropy (UTA) curves and intensities (UTAI) across 25 global cities obtained by this study and by Wang et al. (2022) (termed $UTAI_{GEE}$ and $UTAI_{W}$, respectively) | The subplots (a), (b), (c), and (d) denote the Aqua-based summer daytime UTAI, Terra-based summer daytime UTAI, Aqua-based winter daytime UTAI, and Terra-based winter daytime UTAI, respectively. The δLST denotes the difference between off-nadir and nadir LST, and the VZA denotes the sensor viewing zenith angles (VZAs).

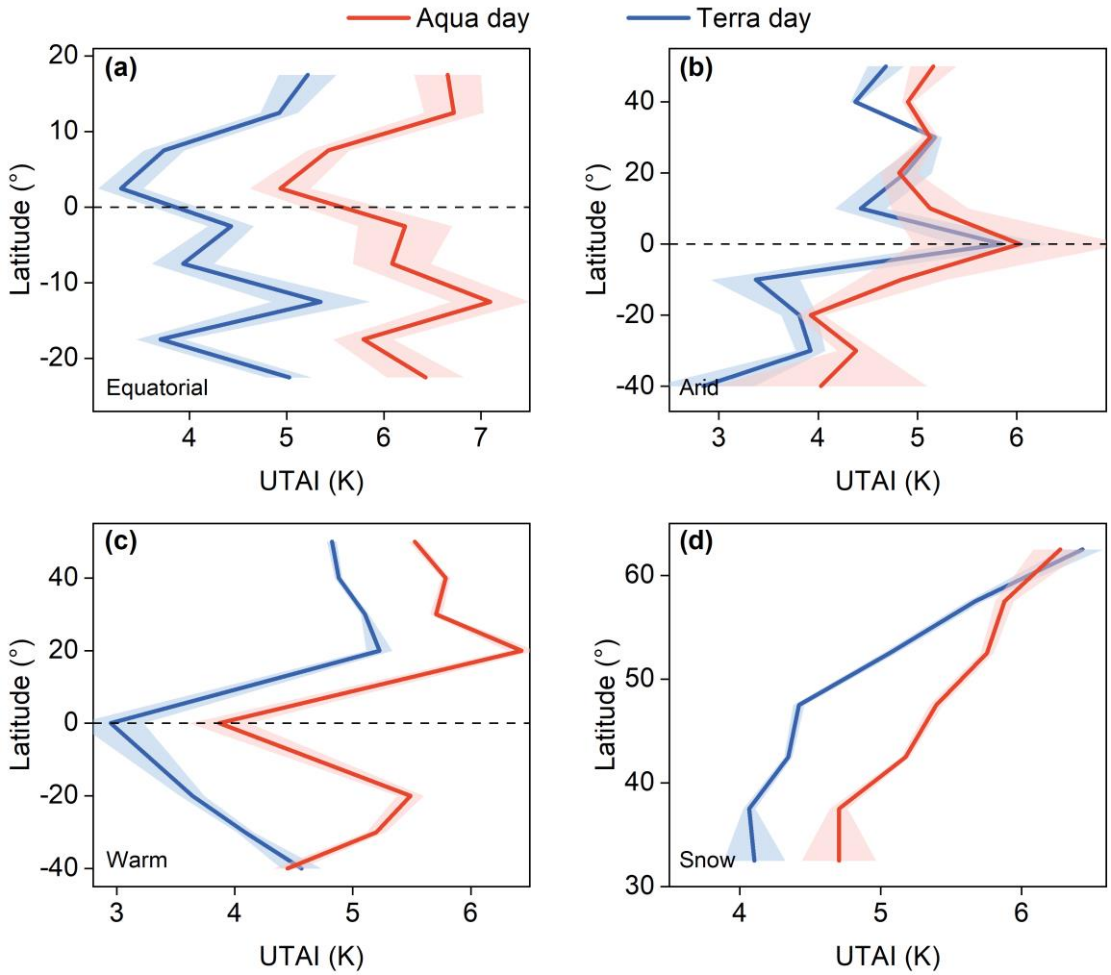

Fig. S10. The latitudinal variations of UTAI across all climate zones during summer daytime.

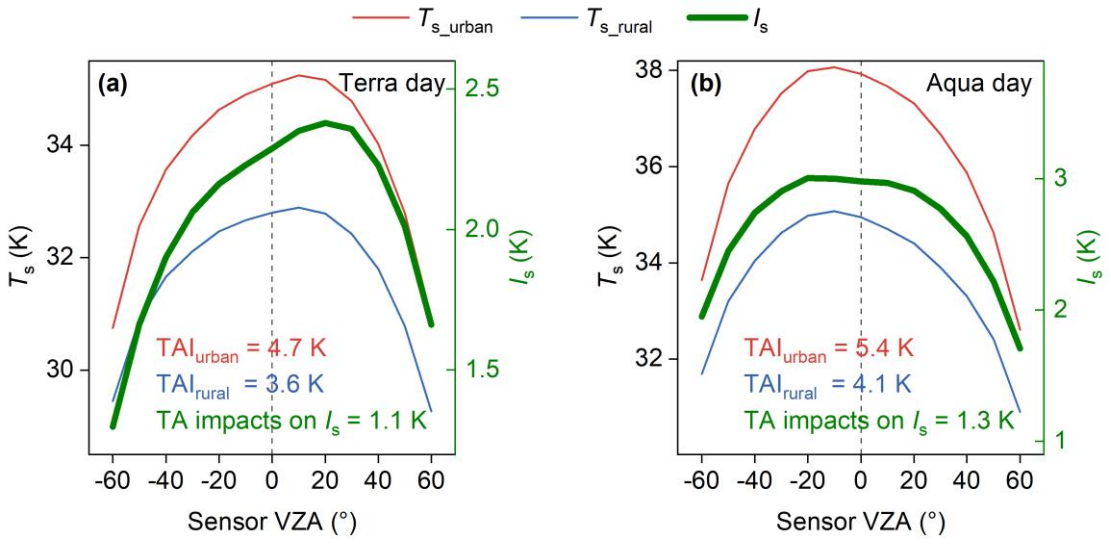

Fig. S11. The thermal anisotropy (TA) patterns during summer daytime over urban surfaces (red curves) and rural surfaces (blue curves) across global cities, as well as the TA impacts on surface UHI intensity (I_s, green curves) for Terra Day (a) and Aqua Day (b) | TAI_{urban} and TAI_{rural} denote the TA intensity (TAI) over urban and rural surfaces, respectively; and T_s and VZA are the land surface temperature and viewing zenith angle, respectively.

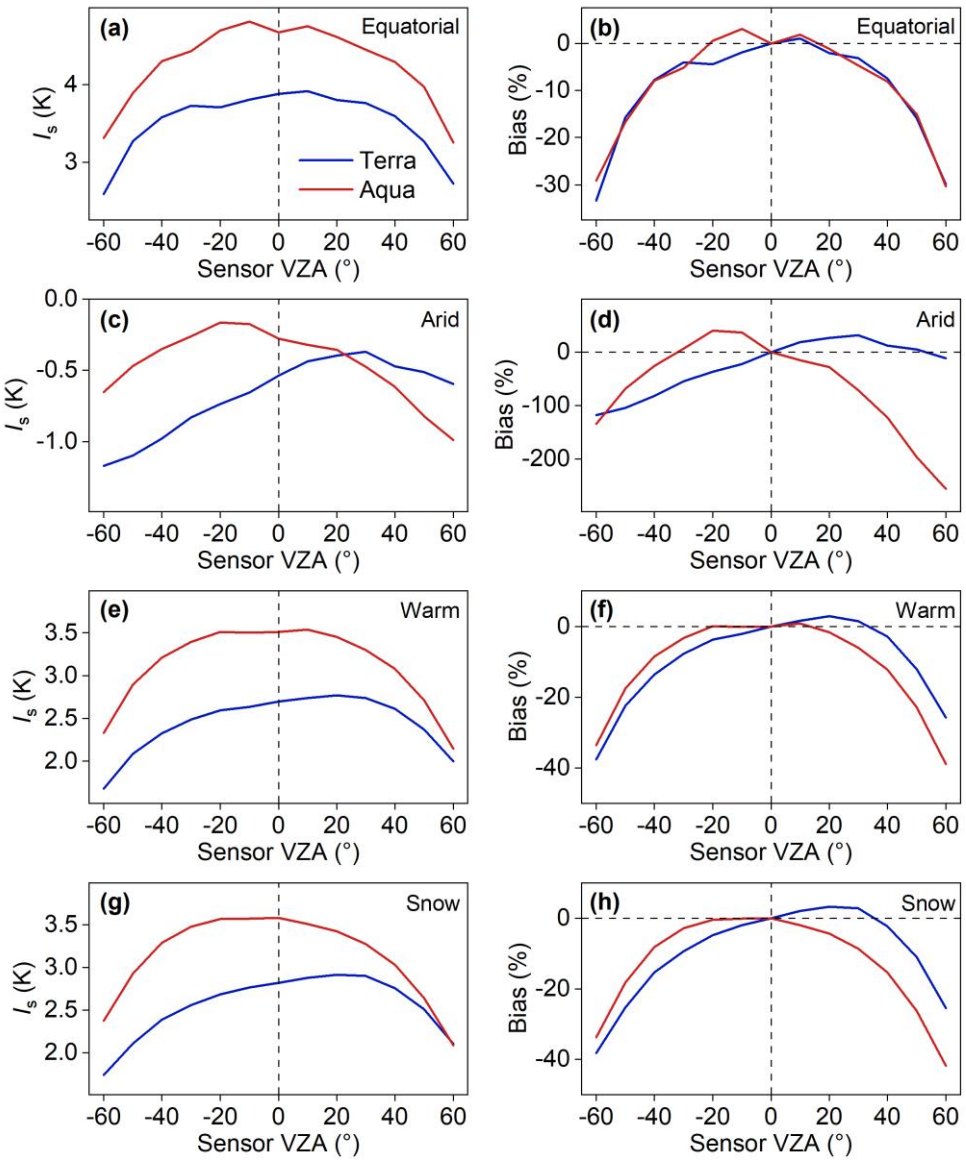

Fig. S12. Variations of summer daytime I_s (a, c, e, and g) and the associated UTA-induced I_s biases with different sensor VZAs (b, d, f, and h) in different

climate zones | The red and blue curves denote the Aqua- and Terra-based results, respectively.

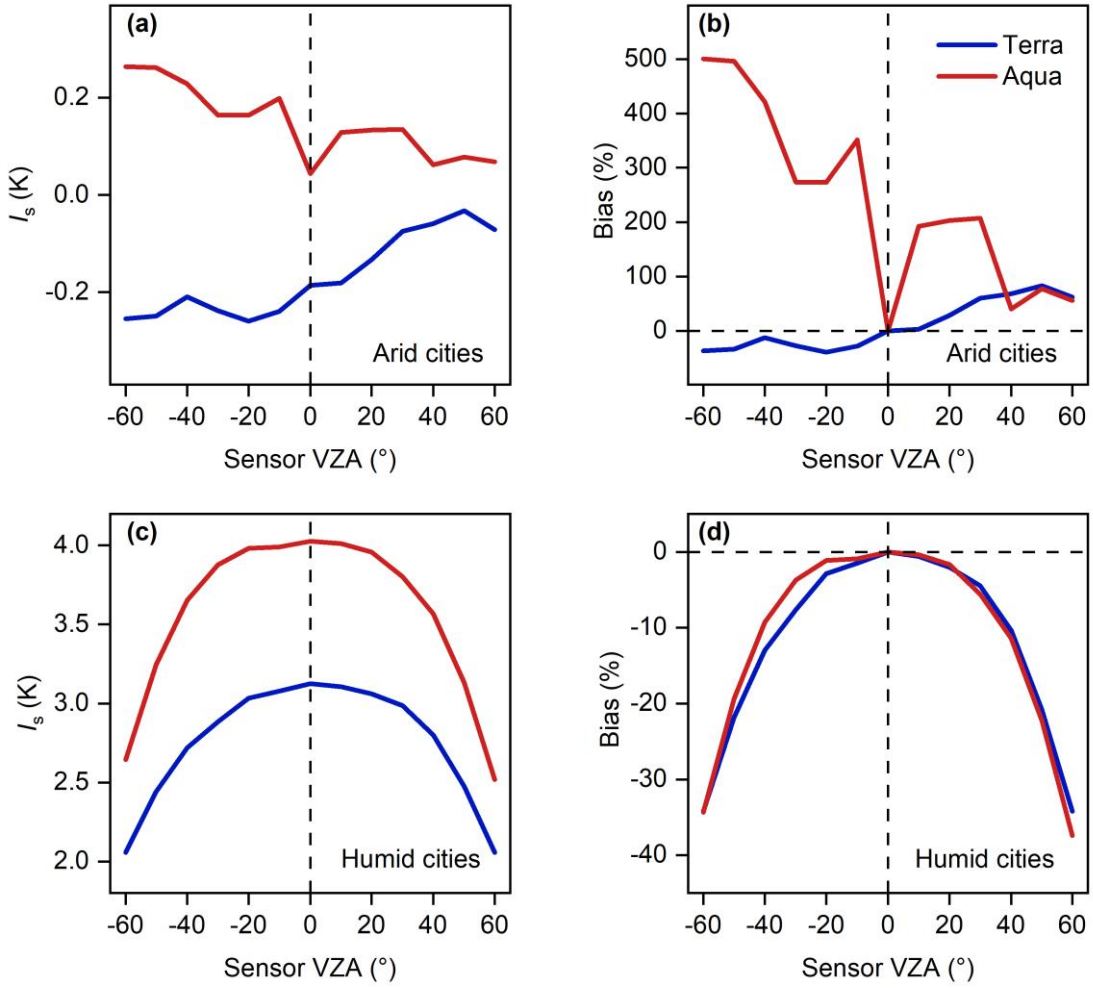

Fig. S13. Variations of summer daytime I_s and the associated UTA-induced I_s biases with different sensor VZAs over arid (a and b) and humid cities (c and d) of North America | The red and blue curves denote the Aqua- and Terra-based results, respectively.

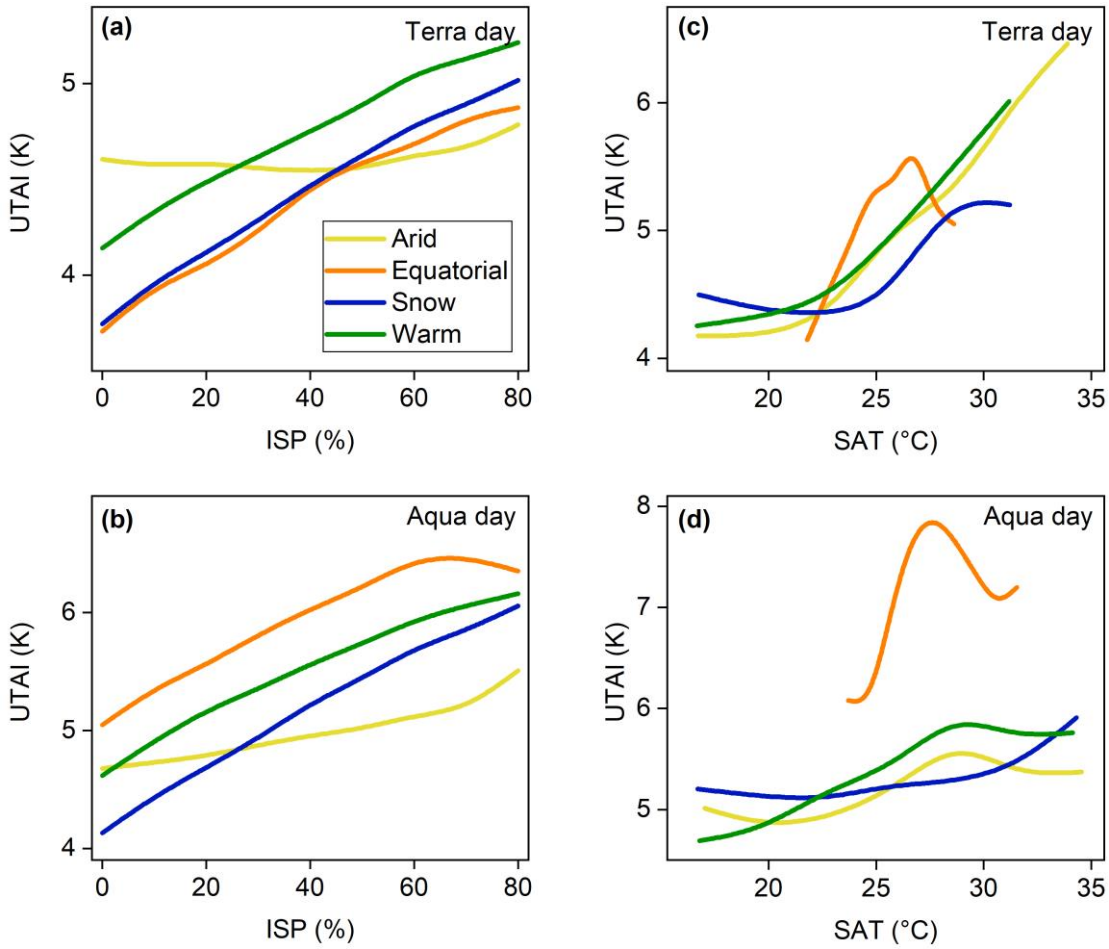

Fig. S14. The summer daytime UTAI variations with different impervious surface percentages (ISPs; a and b) and surface air temperatures (SATs; c and d) across various climate zones.

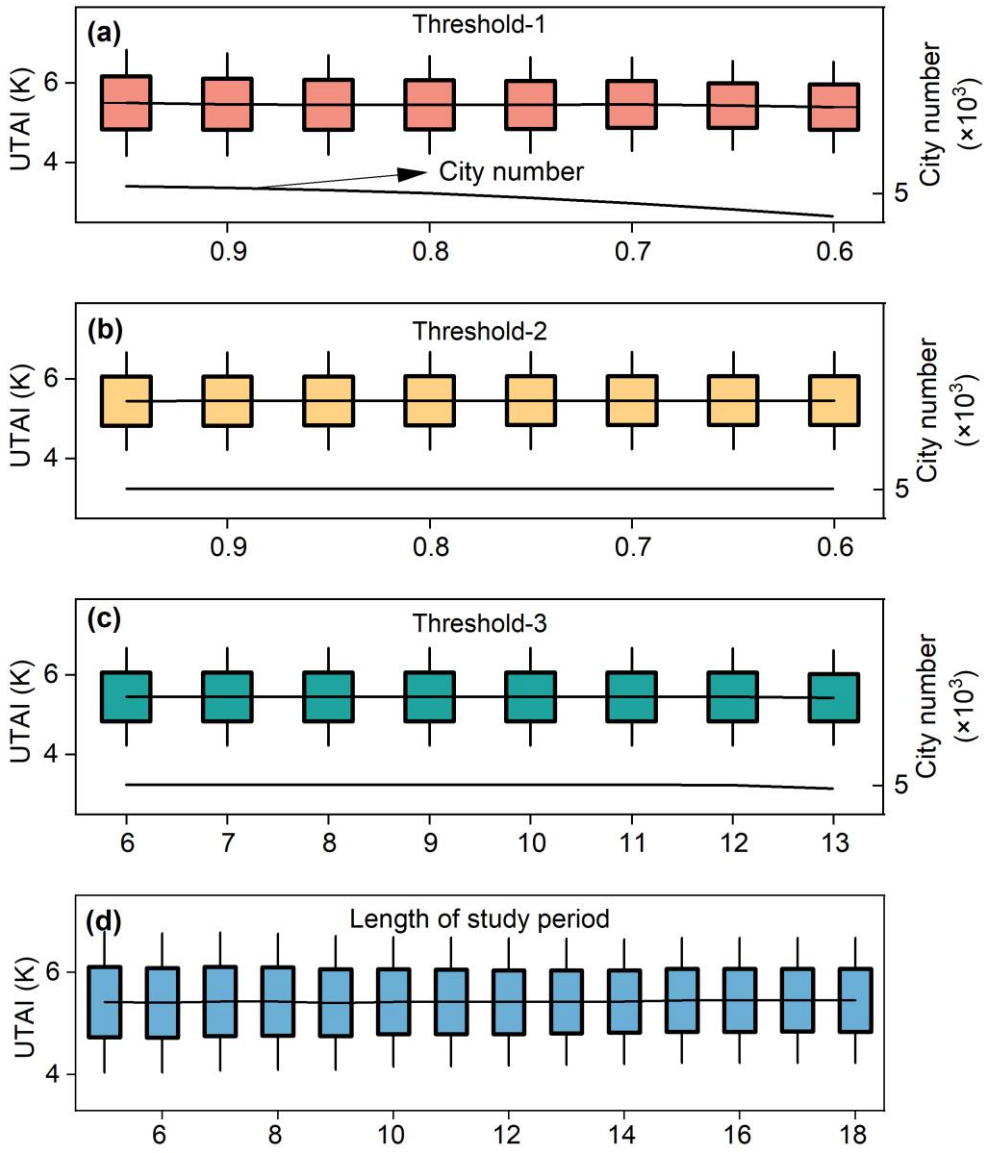

Fig. S15. Quantified impacts from threshold setting and urbanization on the UTAI quantification across global cities | The case for the threshold for filtering clear-sky pixels (denoted by threshold-1; **a**), for selecting usable sensor VZA intervals (threshold-2; **b**), and for choosing usable cities (threshold-3; **c**); the urbanization-induced impacts on the UTAI quantification using MODIS LST observations from 5 to 18 years (**d**).

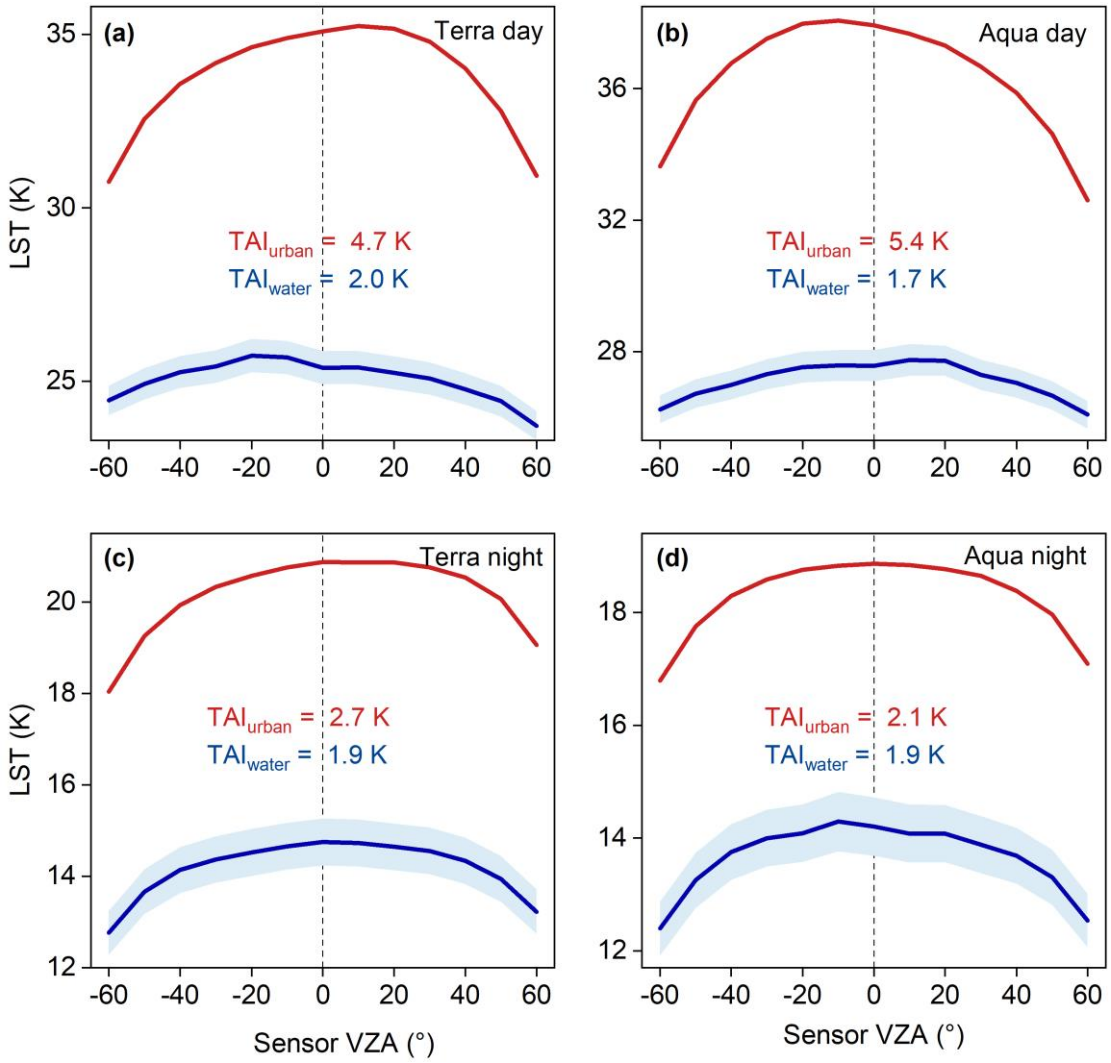

Fig. S16. The thermal anisotropy patterns over urban surfaces and water bodies in the day (a and b) and at night (c and d) | TAI_{urban} and TAI_{water} denote the TAI over urban surfaces and water bodies respectively; and the shades represent the standard errors.

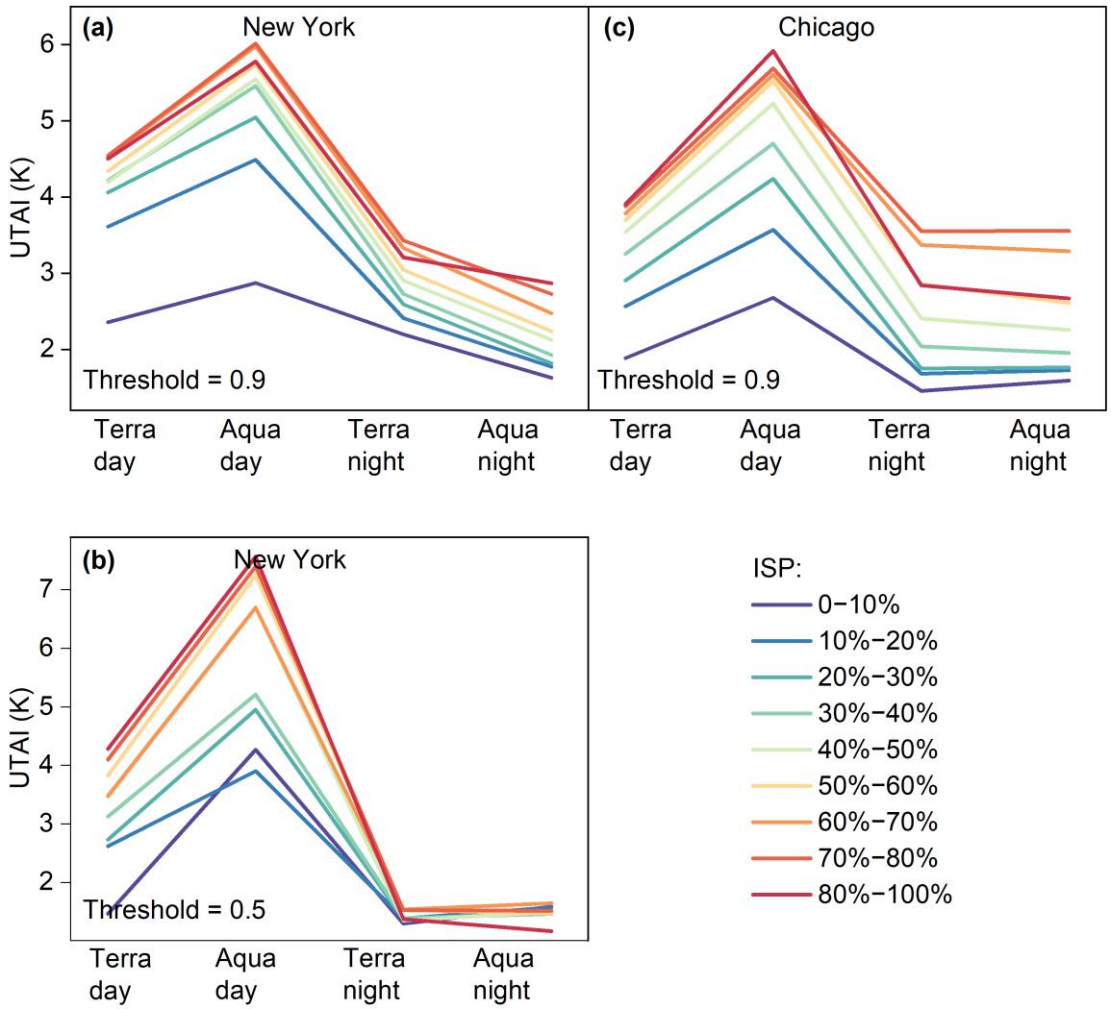

Fig. S17. The UTAI over surfaces with different ISPs in New York (a and b) and Chicago (c) using different thresholds for filtering clear-sky pixels.

C. Supplementary Table

Table S1. Number of cities for the UTA investigation.

Time node	city number
summer Terra day	5374
summer Aqua day	5400
summer Terra night	5287

summer Aqua night	5261
winter Terra day	4143
winter Aqua day	4312
winter Terra night	4872
winter Aqua night	4590

D. Supplementary References

1. Peel MC, Finlayson BL, McMahon TA. Updated world map of the Köppen-Geiger climate classification. Hydrol Earth Syst Sci 2007; 11: 1633–1644.
2. Ermida SL, DaCamara CC, Trigo IF, et al. Modelling directional effects on remotely sensed land surface temperature. Remote Sens Environ 2017; 190: 56–69.
3. Vinnikov KY, Yu YY, Goldberg MD, et al. Angular anisotropy of satellite observations of land surface temperature. Geophys Res Lett 2012; 39: L23802.
4. Wan ZM. Collection-6 MODIS LST user guide. 2013.
5. Friedl M, Sulla Menashe D. MCD12Q1 MODIS/Terra + Aqua Land Cover Type Yearly L3 Global 500m SIN Grid V006. NASA EOSDIS Land Processes DAAC, 2019.
6. Muñoz Sabater J. ERA5-land monthly averaged data from 1981 to present. Copernicus Climate Change Service Climate Data Store 2019; 146: 1999–2049.
7. Li XC, Gong P, Zhou YY, et al. Mapping global urban boundaries from the global artificial impervious area (GAIA) data. Environ Res Lett 2020; 15: 094044.
8. Pesaresi M, Ehrlich D, Ferri S, et al. Global human settlement analysis for disaster risk reduction. International Archives of the Photogrammetry, Remote Sensing & Spatial Information Sciences, 2015.

9. Li MM, Koks E, Taubenböck H, et al. Continental-scale mapping and analysis of 3D building structure. Remote Sens Environ 2020; 245: 111859.
10. Liu ZH, Lai JM, Zhan WF, et al. Urban heat islands significantly reduced by COVID-19 lockdown. Geophys Res Lett 2022; 49: e2021GL096842.
11. Wang DD, Chen YH, Hu LQ, et al. Urban thermal anisotropy: A comparison among observational and modeling approaches at different time scales. IEEE Trans Geosci Remote Sensing 2022; 60: 1–15.
12. Krayenhoff ES, Voogt JA. Daytime thermal anisotropy of urban neighbourhoods: Morphological causation. Remote Sens 2016; 8: 108.
13. Hu LQ, Monaghan A, Voogt JA, et al. A first satellite-based observational assessment of urban thermal anisotropy. Remote Sens Environ 2016; 181: 111–121.
14. Wang DD, Chen YH, Hu LQ, et al. Satellite-based daytime urban thermal anisotropy: A comparison of 25 global cities. Remote Sens Environ 2022; 283: 113312.
15. Ye XM, Xiao XB, Shi JB, et al. The new concepts of measurement error theory. Measurement 2016; 83: 96–105.
16. Li ZL, Tang BH, Wu H, et al. Satellite-derived land surface temperature: Current status and perspectives. Remote Sens Environ 2013; 131: 14–37.
17. Jiang L, Zhan WF, Tu LL, et al. Diurnal variations in directional brightness temperature over urban areas through a multi-angle UAV experiment. Build Environ 2022; 222: 109408.
18. Manoli G, Fatichi S, Schläpfer M, et al. Magnitude of urban heat islands largely explained by climate and population. Nature 2019; 573: 55–60.
19. Voogt JA, Grimmond C. Modeling surface sensible heat flux using surface

radiative temperatures in a simple urban area. J Appl Meteorol Climatol 2000; 39: 1679–1699.